Monthly Notices
of the
ROYAL ASTRONOMICAL SOCIETY

MNRAS **487,** 3392–3403 (2019)
Advance Access publication 2019 June 04

doi:10.1093/mnras/stz1531

The ortho-to-para ratio of water in interstellar clouds

A. Faure,[1★] P. Hily-Blant,[1★] C. Rist,[1] G. Pineau des Forêts,[2,3] A. Matthews[1] and D. R. Flower[4]

[1]*CNRS, IPAG, Univ. Grenoble Alpes, F-38000 Grenoble, France*
[2]*LERMA, UMR 8112 du CNRS, Observatoire de Paris, Ecole Normale Supérieure, 61 Av. de l'Observatoire, F-75014 Paris, France*
[3]*IAS, UMR8617 du CNRS, Université de Paris Sud, F-91705 Orsay, France*
[4]*Physics Department, The University, Durham DH1 3LE, UK*

Accepted 2019 May 29. Received 2019 May 28; in original form 2019 April 9

ABSTRACT

The nuclear-spin chemistry of interstellar water is investigated using the *University of Grenoble Alpes Astrochemical Network* (UGAN). This network includes reactions involving the different nuclear-spin states of the hydrides of carbon, nitrogen, oxygen, and sulphur, as well as their deuterated forms. Nuclear-spin selection rules are implemented within the scrambling hypothesis for reactions involving up to seven protons. The abundances and ortho-to-para ratios (OPRs) of gas-phase water and water ions (H_2O^+ and H_3O^+) are computed under the steady-state conditions representative of a dark molecular cloud and during the early phase of gravitational collapse of a pre-stellar core. The model incorporates the freezing of the molecules on to grains, simple grain surface chemistry, and cosmic ray induced and direct desorption of ices. The predicted OPRs are found to deviate significantly from both thermal and statistical values and to be independent of temperature below ∼30 K. The OPR of H_2O is shown to lie between 1.5 and 2.6, depending on the spin state of H_2, in good agreement with values derived in translucent clouds with relatively high extinction. In the pre-stellar core-collapse calculations, the OPR of H_2O is shown to reach the statistical value of 3 in regions with severe depletion ($n_H > 10^7$ cm^{-3}). We conclude that a low water OPR ($\lesssim 2.5$) is consistent with gas-phase ion-neutral chemistry and reflects a gas with OPR(H_2) $\lesssim 1$. Available OPR measurements in protoplanetary discs and comets are finally discussed.

Key words: astrochemistry – molecular data – molecular processes – ISM: abundances – ISM: molecules.

1 INTRODUCTION

The origin and distribution of water in the Solar system is not well understood. In particular, the fraction of pristine i.e. unprocessed interstellar water in comets and asteroids remains poorly constrained. The contribution of comets and asteroids to the water accreted by Earth is in turn a long-standing problem (Alexander, McKeegan & Altwegg 2018). Yet these questions are critical to understanding star and planet formation in general and to assessing how typical is the Solar system. Water is the second most abundant molecule (after H_2) in the Solar system and is also an essential ingredient for life on Earth.

Isotopic fractionation, i.e. the enrichment or depletion of an isotope in a molecule relative to its elemental abundance, provides a powerful diagnostic tool for tracing the chemical history of the Solar system. For instance, the water D/H and $^{18}O/^{16}O$ ratios in the coma of comet 67P/Churyumov–Gerasimenko were measured recently by the ROSINA mass spectrometer onboard the *Rosetta* spacecraft. Both ratios were found to be enriched with respect to the terrestrial values, in agreement with the scenario where 67P's water was inherited unprocessed from the pre-solar cloud (Altwegg et al. 2017; Schroeder et al. 2018). In particular, the HDO/H_2O and D_2O/HDO ratios, respectively 1.05×10^{-3} (more than three times the terrestrial value) and 1.8×10^{-2}, were found to be similar to values reported for low-mass protostars embedded in molecular clouds (see Altwegg et al. 2017, and reference therein). Additionally, disc models have shown that unlike molecular clouds, the solar nebula protoplanetary disc was probably unable to efficiently produce deuterium-rich water (Cleeves et al. 2014). These studies thus suggest that a significant fraction of the Solar system's water is interstellar in origin (see also van Dishoeck et al. 2014).

Likewise, the ortho-to-para ratio (OPR) of H_2O might be used as an alternative tool to trace the link between interstellar, cometary, and planetary water. With its two equivalent hydrogen atoms,

★ E-mail: alexandre.faure@univ-grenoble-alpes.fr (AF);
pierre.hily-blant@univ-grenoble-alpes.fr (PHB)

H_2O exists in the form of two distinct nuclear-spin isomers, para ($I = 0$, where I is the total nuclear spin) and ortho ($I = 1$), whose interconversion in the gas phase via radiative and inelastic collisional transitions is forbidden or very slow. The statistical or high-temperature OPR of H_2O is 3 and any OPR lower than 3 can be interpreted in terms of an equilibrium *spin temperature*. In comets, the spin temperature has been traditionally considered as a proxy for the formation temperature of water ice (Mumma et al. 1986; Bonev et al. 2013). Typical values for the OPR of H_2O in comets lie in the range 2–3, corresponding to spin temperatures lower than 50 K (see Faggi et al. 2018, and references therein). In the interstellar medium (ISM), it is generally believed that the OPR of water formed in the gas phase should be statistical i.e. equal to 3. The OPR of H_2O in the ISM was accurately measured using the HIFI spectrometer onboard the *Herschel* space observatory. In diffuse and translucent clouds the OPR of H_2O is usually consistent with the statistical value, but values in the range 2–3 have also been reported (see van Dishoeck, Herbst & Neufeld 2013, and references therein). In protoplanetary discs, an accurate measure is not available but estimates are consistent with the interstellar and cometary range of 2–3 (Pontoppidan et al. 2010; Salinas et al. 2016). In the cold and dense ISM, only the ground-state oH_2O transition was detected towards the L1544 pre-stellar core (Caselli et al. 2012), thus precluding a measure of the OPR.

In summary, many H_2O OPR measurements are now available for comets and interstellar clouds, but their meaning remains unclear. In addition, the above assumptions linking the spin state of a molecule to its formation process have been recently challenged by both experiment and theory. First, the OPR of H_2O photodesorbed and thermally desorbed from ice at 10 and 150 K, respectively, was found equal to the statistical value of 3, even when the ice was produced *in situ* at 10 K (Hama, Kouchi & Watanabe 2016) and when the ice was made from pH_2O monomers (Hama, Kouchi & Watanabe 2018). The assumed relation between the OPR and the formation temperature of water ice is thus not supported experimentally. Second, the existence of nuclear-spin selection rules in chemical reactions, as predicted theoretically by Quack (1977), has been demonstrated experimentally in ion-neutral reactions involving H_3^+ (Uy, Cordonnier & Oka 1997; Crabtree et al. 2011b). The nuclear-spin chemistry of interstellar molecules has gained interest in recent years and detailed models have been dedicated to the OPR of NH_3 (Faure et al. 2013; Le Gal et al. 2014), H_3^+ and its deuterated isotopologues (Albertsson et al. 2014; Harju et al. 2017b), deuterated ammonia (Harju et al. 2017a), H_2O^+ (Herbst 2015) and H_2Cl^+ (Neufeld et al. 2015; Le Gal et al. 2017). These studies have shown that the OPR of molecules formed in the gas phase can be significantly lower than the statistical (high-temperature limit) values and is entirely controlled by chemical selection rules.

In this work, we investigate the nuclear-spin chemistry of gas-phase water from interstellar clouds ($T \leq 100$ K) to cold pre-stellar cores ($T \sim 10$ K). Our model is based on the *University of Grenoble Alpes Astrochemical Network* (UGAN) as recently published by Hily-Blant et al. (2018; hereafter HB18). This network includes the nuclear-spin states of H_2, H_2^+, H_3^+ and of all the hydrides of carbon, nitrogen, oxygen, and sulphur, as well as their abundant deuterated forms. It was used by HB18 to study the deuterated isotopologues of ammonia in collapsing pre-stellar sources.

In Section 2, we summarize the update of the UGAN network for the water chemistry. Section 3 contains our results both for the steady-state composition of a molecular cloud with uniform density and temperature and for a collapsing core. Comparison with available observations is discussed in Section 4 and Section 5 gives our concluding remarks.

2 THE MODELS

The aim of this work is to compute the abundance and OPR of H_2O (and its precursors) under the steady-state conditions representative of a dark molecular cloud and also during the initial stage of gravitational collapse of a pre-stellar core, which ultimately leads to the formation of a low-mass protostar. The dynamical model was presented in HB18 and derives from the studies of gravitational collapse by Larson (1969) and Penston (1969). Briefly, the collapsing core loses mass to the surrounding envelope at a rate that ensures that the density profile in the envelope is proportional to $R_{\rm env}^{-2}$, where $R_{\rm env}$ is the envelope radius. Full details can be found in HB18. This dynamical model is combined with the UGAN chemical network, also presented in HB18, which is an upgraded version of the gas-phase network of Flower, Pineau des Forêts & Walmsley (2006; hereafter F06). The F06 network included reactions involving species containing H, D, He, C, N, O, and S and distinguished between the different nuclear-spin states of H_2, H_2^+, H_3^+ (including deuterated forms) and between those of nitrogen hydrides. A first update of the F06 network consisted in a revision of the nitrogen-hydrides' chemistry (excluding deuterated species) (Le Gal et al. 2014). In particular, the nuclear-spin selection rules were derived with the method of Oka (2004), which is based on the conservation of the rotational symmetry of the nuclear-spin isomers. These symmetry rules depend upon the mechanism of reaction, and two extreme mechanisms can be considered: hopping and scrambling. In HB18, scrambling was assumed because at very low temperature, ion-neutral reactions usually form long-lived intermediate complexes in which complete randomization of H and/or D atoms can take place, as shown experimentally (Crabtree et al. 2011b). The second update by HB18 consisted of extending the work of Le Gal et al. (2014) to the entire F06 network in a systematic fashion for all hydrides containing C, N, O, and S atoms, and their deuterated forms. To this end, the nuclear-spin selection rules were derived from the permutation symmetry approach of Quack (1977), which is more general and adapted to deuterium nuclei. The nuclear-spin separation procedure is described in detail in HB18. Finally, many reaction rate coefficients were updated from a literature survey.

We describe below the third update of the F06 network which mainly consists of a revision of the oxygen hydrides chemistry.

2.1 Water chemistry

The chemistry of interstellar water can follow three distinct routes (van Dishoeck et al. 2013): (i) low-temperature ion-neutral gas-phase chemistry ($T \leq 100$ K), (ii) high-temperature neutral–neutral gas-phase chemistry, and (iii) surface chemistry. In this work, the first and third routes are included but surface reactions are treated in a very simple fashion (see Section 2.2 below).

The low-temperature ion-neutral synthesis of H_2O starts with the ionization of H_2 by cosmic ray protons and secondary electrons. This leads to H, H^+, and H_2^+ and also to H_3^+ via the fast reaction between H_2 and H_2^+. Oxygen atoms react with either H^+ to create O^+ ions (by charge transfer) or with H_3^+ to form

OH^+ and H_2O^+:

$$O + H^+ \rightarrow O^+ + H \quad (1)$$

$$O^+ + H_2 \rightarrow OH^+ + H \quad (2)$$

$$O + H_3^+ \rightarrow OH^+ + H_2 \text{ or } H_2O^+ + H \quad (3)$$

Water is then formed via a small chain of exothermic and barrierless reactions:

$$OH^+ + H_2 \rightarrow H_2O^+ + H \quad (4)$$

$$H_2O^+ + H_2 \rightarrow H_3O^+ + H \quad (5)$$

$$H_3O^+ + e^- \rightarrow H_2O + H \quad (6)$$

It should be noted that because the formation of H^+ and H_3^+ is initiated by the cosmic ray ionization of H_2, the formation of OH^+, H_2O^+, and H_3O^+ is essentially cosmic ray driven and their relative abundance can be used to constrain the cosmic ray ionization rate (Hollenbach et al. 2012; Indriolo et al. 2015).

The rate coefficients for reactions (1), (3), and (6) are those of HB18. The rate coefficient for reaction (1), averaged over the fine-structure levels of oxygen, is taken from the drift-tube measurements of Federer et al. (1984) at 300 K. Theoretical calculations by Chambaud et al. (1980), Stancil et al. (1999), and Spirko, Zirbel & Hickman (2003) are in good agreement and they all lie within the experimental error bar (±50 per cent). However, the theoretical results differ significantly from each other at the state-to-state level, especially when the oxygen atom is in the ground state ($^3P_2$). State-resolved experimental data below 100 K would be very useful to resolve the disagreement between the calculations. This is particularly important where most oxygen atoms are in the ground state The rate coefficient for reaction (3) is taken from the transition state theory calculations of Klippenstein, Georgievskii & McCall (2010) and it was combined with the experimental branching ratios determined by Milligan & McEwan (2000) at 300 K. The rate coefficient and branching ratios for reaction (6) are taken from the storage ring measurements of Jensen et al. (2000), which agree well with the most recent results of Buhr et al. (2010) for D_3O^+.

The rate coefficients for reactions (2), (4), and (5) have been updated using very recent experimental studies performed at low temperatures. Reaction (2) was studied by Kovalenko et al. (2018) in a ion trap down to 15 K and it was found to be almost temperature independent. The rate coefficient is taken here as the value measured at 15 K, i.e. 1.3×10^{-9} cm^3 s^{-1}, with no temperature dependence. Reactions (4) and (5) were studied in ion traps by both Tran et al. (2018) and Kumar et al. (2018). Again the temperature dependence was found to be small and the rate coefficients are taken as the values measured at 21 K by Kumar et al. (2018) i.e. 1.22×10^{-9} cm^3 s^{-1} for reaction (4) and 1.57×10^{-9} cm^3 s^{-1} for reaction (5), with no temperature dependence. These values are in good agreement with ring polymer calculations performed by Kumar et al. (2018) and agree also with the independent measurements of Tran et al. (2018), within typically 30 per cent. These new measurements confirm that O^+, OH^+, and H_2O^+ ions react very fast with molecular hydrogen down to interstellar temperatures, with rate coefficients close to the Langevin limit.

Finally, the above rate coefficients were duplicated to consistently update the deuterated homologues of reactions (1)–(6). In this 'cloning' procedure, the overall rate coefficients of the deuterated reactions are assumed to be the same as the original (hydrogenated) reactions, except when isotope measurements are available. This point is further discussed in Section 3.1.4 below.

2.2 Grain-surface processes

Grain-surface reactions are not explicitly included in the UGAN network, except the formation (and immediate desorption) of H_2 and isotopologues. The rates of adsorption of neutral species include the contribution of the ice mantle thickness to the grain cross-section, as described in the appendix B of Walmsley, Flower & Pineau des Forêts (2004). All oxygen atoms from the neutral species O, OH, H_2O, NO, SO, and SO_2 are assumed to form water ice once they are adsorbed by the grains. The list of species formed in grain mantles is given in the table D1 of HB18.

The desorption of molecules by the cosmic ray induced ultraviolet radiation field is included and described in the appendix A of HB18. Our treatment of desorption induced by direct cosmic ray impact follows the formulation of Flower, Pineau des Forêts & Walmsley (2005, see their section 3.3). Briefly, the rate of desorption of species i (averaged over the cosmic ray flux) per unit volume per unit time from the grains is

$$R_i^{\rm crd} = \frac{n_i^{\rm g}}{\sum_i n_i^{\rm g}} n_{\rm g} \pi a_{\rm g}^2 \gamma_{\rm CO} \exp\left[\frac{-(E_i^{\rm ads} - E_{\rm CO}^{\rm ads})}{T_{\rm g}^{\rm max}}\right], \quad (7)$$

where $\frac{n_i^g}{\sum_i n_i^g}$ is the fractional abundance of species i on grains, $n_{\rm g}$ is the number density of grains of radius $a_{\rm g}$, $\gamma_{\rm CO}$ is the CO yield averaged over the cosmic ray flux (in molecules cm^{-2} s^{-1}), $E_i^{\rm ads}$ is the adsorption energy of the species (as a pure ice), and $T_{\rm g}^{\rm max}$ is the maximum temperature reached by the grains following cosmic ray impact. This formulation is similar (but simpler) than that of Hasegawa & Herbst (1993). It assumes, in particular, an exponential dependence of the desorption rate on adsorption energy, as for thermal evaporation. Following Flower et al. (2005), we adopted $T_{\rm g}^{\rm max} = 70$ K, as derived by Hasegawa & Herbst (1993). For the CO yield (in molecules cm^{-2} s^{-1}) we used $\gamma_{\rm CO} = 70\ \zeta_{17}$ where ζ_{17} is the rate of cosmic ray ionization of molecular hydrogen in unit of 10^{-17} s^{-1}. This value for $\gamma_{\rm CO}$ was derived by Léger, Jura & Omont (1985) for 'spot' heating (i.e. sputtering) of grain mantles. In the case of species with high adsorption energies like water and ammonia, however, the above formulation underestimates the desorption rates by orders of magnitude (Bringa & Johnson 2004). In fact, the desorption rate for such species is dominated by the 'prompt' or very early desorption which does not scale as $\exp(-E_i^{\rm ads})$. Bringa & Johnson (2004) have suggested a scaling $R_i^{\rm crd} \propto (E_i^{\rm ads})^{-m}$ with $m \sim 2$. For H_2O (and isotopologues), $\gamma_{\rm H_2O}$ was thus directly computed from experimental data (see Appendix A). We obtained $\gamma_{\rm H_2O} = 0.8\ \zeta_{17}$, i.e. about a factor of 100 smaller than $\gamma_{\rm CO}$. For NH_3 (and isotopologues), we adopted the same formulation as for H_2O with $\gamma_{\rm NH_3} = (E_{\rm H_2O}^{\rm ads}/E_{\rm NH_3}^{\rm ads})^2 \gamma_{\rm H_2O} = 2.96\ \gamma_{\rm H_2O}$ molecules cm^{-2} s^{-1} using binding energies from Brown & Bolina (2007). For all other species, equation (7) was employed.

Taking typical conditions for dark molecular clouds ($n_{\rm H} = 10^4$ cm^{-3}, $\zeta = 3 \times 10^{-17}$ s^{-1}, $n_{\rm g} = 1.7 \times 10^{-8}$ cm^{-3}, $\sum_i n_i^{\rm g} = 1.9$ cm^{-3} , $a_{\rm g} = 0.13$ μm), the desorption rates per unit time for CO and H_2O are $k_{\rm CO}^{\rm crd} \sim 9.5 \times 10^{-16}$ s^{-1} and $k_{\rm H_2O}^{\rm crd} \sim 1.1 \times 10^{-17}$ s^{-1}, which agree within a factor of ∼2–4 with the 'experimental' rates derived by Bringa & Johnson (2004). The corresponding time-

scales are $t_{CO}^{crd} \sim 3.3 \times 10^7$ yr and $t_{H_2O}^{crd} \sim 2.3 \times 10^9$ yr, which are both longer than the typical lifetime of a molecular cloud. We note that $t_{H_2O}^{crd}$ is very similar to the time-scale for cosmic ray induced photodesorption ($\sim 10^9$ yr, see Hily-Blant et al. 2018), meaning that the two processes are in competition and will become significant at the higher densities of pre-stellar cores (see Section 3.2).

Finally, a gas-phase OPR equal to the statistical (high-temperature) value is assumed for all species upon cosmic ray (induced and direct) desorption, as suggested by the photodesorption experiments of Hama et al. (2018). Thus, whatever the mechanism, a water molecule desorbed from ice will have an initial OPR of 3 once in the gas phase.

3 RESULTS

The initial distribution of the elements is specified in tables 2 and 3 of HB18. In particular, the fractional abundance of oxygen atoms (relative to the total H nuclei density n_H) in the gas phase is 1.24×10^{-4} and that of H_2O molecules in the grain mantles is 1.03×10^{-4}. A discussion on the uncertainties surrounding the elemental abundances can be found in Le Gal et al. (2014).

3.1 Steady-state composition

We first investigate the steady-state abundances of oxygenated species for an interstellar cloud having a uniform density ($n_H = 10^4$ cm^{-3}) and kinetic temperature (T) in the range 5–100 K. The cosmic ray ionization rate of H_2 is taken as $\zeta = 3 \times 10^{-17}$ s^{-1} in our reference model, which is close to the average rate inferred from molecular ion observations in dense clouds (see Indriolo & McCall 2012, and references therein). We have also studied the impact of a larger rate, $\zeta = 3 \times 10^{-16}$ s^{-1}, more representative of diffuse or translucent clouds (Neufeld & Wolfire 2017). The initial radius of the refactory grain core is taken as 0.1 μm. It should be noted that in these steady-state runs, grain surface processes are turned off so that the mantle composition (see table 3 of HB18) is fixed and most of the oxygen is locked into ices (mainly water). We have also ignored the presence of an external far-ultraviolet (FUV) field so that the results below are most relevant for interstellar clouds with moderate to high extinction ($\gtrsim$3 mag.), i.e. from translucent to dark cloud conditions. In particular, the molecular hydrogen fraction ($f_{H_2} = 2n(H_2)/n_H$) is close to unity and the electron fraction is lower than 3×10^{-7} in our simulations. The temperature is varied from 5 to 100 K to explore a large range of OPRs of H_2 (see below).

Table 1 presents the steady-state abundances of several species related to H_2O at 10 K and for two values of ζ. We first notice that the fractional abundance of H_2O is $\sim 3.5 \times 10^{-7}$. This value is similar to the H_2O peak abundance in the elaborate photodissociation region (PDR) models of Hollenbach et al. (2009). In these models, the water peak occurs at visual extinctions $A_V \sim$ 3–8, depending on the incident FUV field. When averaged through the cloud, the H_2O abundance becomes $\sim 10^{-8}$ (Hollenbach et al. 2009), in good agreement with observations of diffuse and translucent clouds (see van Dishoeck et al. 2013, and references therein). In our model, when $\zeta = 3 \times 10^{-16}$ s^{-1}, the abundances of OH^+, H_2O^+, and H_3O^+ are lower but within a factor of 3–10 of those in Hollenbach et al. (2012) at the 'second' peak, i.e. $A_V \sim 5$ (see their fig. 5).

In our model the abundances of O, O_2, H_2O, and H_3O^+ do not strongly vary with ζ (see Table 1). In contrast, the abundances of OH^+ and H_2O^+ are found to scale roughly linearly with ζ (similarly to H_3^+). This was previously discussed by Hollenbach et al. (2012). As a direct consequence, the OH abundance is multiplied by a factor of $\sim$5, decreasing the H_2O/OH ratio from 2 to 0.4. In diffuse and translucent clouds, this ratio lies in the range 0.3–1 (Wiesemeyer et al. 2012). We note that our model predicts that most of the gas-phase oxygen (apart from CO) is in O and O_2. The predicted abundance of O_2 is significantly larger than the observed values, which is an old problem in astrochemistry (Goldsmith et al. 2011).

Table 1. Steady-state abundances expressed relative to $n_H = n(H) + 2n(H_2) = 10^4$ cm^{-3}. The kinetic temperature is fixed at 10 K. Two values of the cosmic ray ionization rate ζ (in s^{-1}) have been used. Numbers of parentheses are powers of 10.

Species	$\zeta = 3 \times 10^{-17}$	$\zeta = 3 \times 10^{-16}$
H	6.9(−05)	7.6(−04)
pH_2	5.0(−01)	5.0(−01)
oH_2	5.4(−04)	8.7(−04)
pH_3^+	4.1(−09)	3.0(−08)
oH_3^+	1.8(−09)	1.5(−08)
O	2.1(−05)	2.9(−05)
OH	1.7(−07)	8.6(−07)
O_2	9.6(−06)	6.1(−06)
pH_2O	1.4(−07)	1.5(−07)
oH_2O	2.1(−07)	2.2(−07)
OH^+	3.2(−13)	3.2(−12)
pH_2O^+	1.6(−13)	1.6(−12)
oH_2O^+	1.8(−13)	1.9(−12)
pH_3O^+	2.3(−09)	4.3(−09)
oH_3O^+	5.6(−10)	1.0(−09)
e^-	4.2(−08)	2.2(−07)

Table 2. Steady-state OPRs of the nuclear-spin isomers listed in Table 1. The kinetic temperature is fixed at 10 K. Two values of the cosmic ray ionization rate ζ (in s^{-1}) have been used. Numbers of parentheses are powers of 10. Thermal (at 10 K) and statistical OPRs are also provided.

Species	$\zeta = 3 \times 10^{-17}$	$\zeta = 3 \times 10^{-16}$	Thermal	Stat.
H_2	1.1(−03)	1.8(−03)	3.5(−07)	3
H_3^+	0.43	0.52	0.075	1
H_2O	1.5	1.5	0.31	3
H_2O^+	1.2	1.2	19	3
H_3O^+	0.24	0.24	0.94	1

The OPRs of the nuclear-spin isomers listed in Table 1 are given in Table 2. We can first observe significant deviations from thermal values. The OPR of H_2, in particular, is suprathermal and corresponds to a spin temperature of $\sim$20 K. We note that the value predicted for H_2O^+ (1.2) is forbidden in thermal equilibrium because the thermal OPR of H_2O^+ is necessarily larger than 3. This is analogous to the case of NH_3 whose OPR is predicted to be lower than unity at low temperature (Faure et al. 2013). The OPRs of water and its ions are found to be insensitive to ζ. We have checked that they are also insensitive to the gas-phase abundance of sulphur, which controls the fractional ionization when ζ is fixed.

3.1.1 *Temperature dependence*

In Fig. 1, the OPRs of H_2 and H_3^+ are plotted as function of the kinetic temperature. Below $\sim$20 K, these ratios are suprathermal and almost independent of temperature: the OPR of H_2 is $\sim 10^{-3}$ and that of H_3^+ $\sim$0.4. In this temperature regime, the formation of oH_2 on the grains is faster than the gas-phase conversion from pH_2 to oH_2 (due to proton exchanges with H^+, H_3^+, and HCO^+). A 'critical' temperature T_{crit} was defined in Faure et al. (2013) to quantitatively

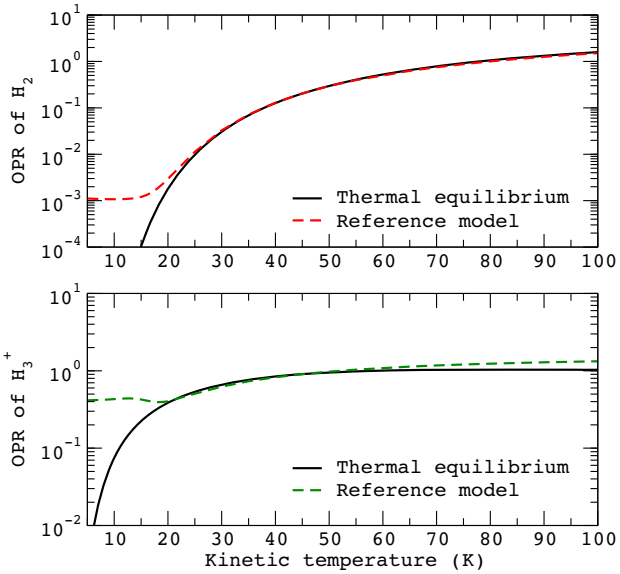

Figure 1. OPRs of H_2 and H_3^+ as function of kinetic temperature. The solid lines give the thermalized OPRs. The dashed lines correspond to our reference model.

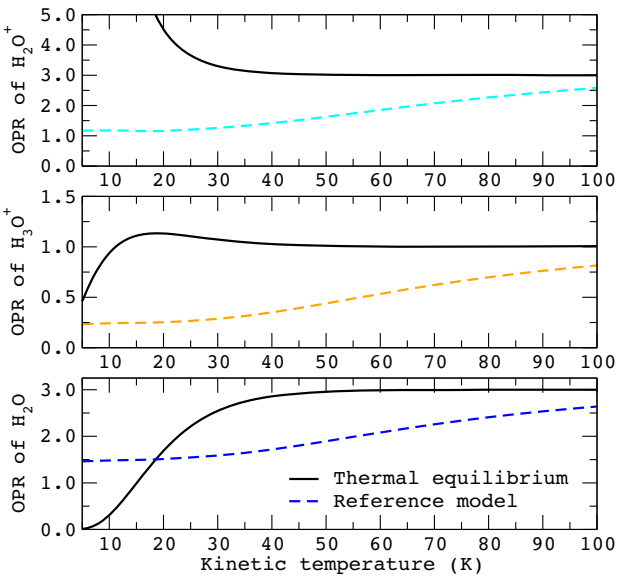

Figure 2. OPRs of H_2O^+, H_3O^+, and H_2O as function of kinetic temperature. The solid lines give the thermalized OPRs. The dashed lines correspond to our reference model.

explain this effect (see their equation 6). Thus, above $T_{crit} \sim 20$ K, the OPR of H_2 rapidly reaches thermal equilibrium because the nuclear-spin conversion rate of H_2 becomes faster than the formation rate. It should be noted that for the equilibration reaction $H_3^+ + H_2$, we have adopted *species-to-species* rate coefficients, as computed by HB18 from the data of Hugo, Asvany & Schlemmer (2009) with the assumption that rotational populations are at local thermal equilibrium (LTE). As a result, above 20 K, not only the OPR of H_2 but also that of H_3^+ reaches thermal equilibrium in our model. In fact, small deviation can be seen at high temperatures because the state-to-state data of Hugo et al. (2009) are strictly valid up to 50 K only.

It is instructive to compare these results with values inferred from infrared and ultraviolet absorption observations. The OPR of H_2 has been measured in diffuse clouds with values ranging from ∼0.3 to 1.5, i.e. spin temperatures between 50 and 100 K (see Crabtree et al. 2011a, and references therein). In dense clouds, H_2 is very difficult to detect and, to our knowledge, the only (published) direct measurements are upper limits reported by Lacy et al. (1994) towards NGC 2024 (OPR < 0.8) and by Goto, Geballe & Usuda (2015) towards NGC 7538 IRS 1 (OPR < 2.3), which are consistent with indirect estimates (see e.g. Troscompt et al. 2009; Dislaire et al. 2012, and references therein). The OPR of H_3^+ has been measured in both dense (McCall et al. 1999) and diffuse clouds (Crabtree et al. 2011a) with values in the range 0.4–1, corresponding to spin temperatures ∼20–50 K for both types of clouds. In diffuse clouds where both H_2 and H_3^+ have been detected, the average H_2 spin temperature is ∼60 K while that of H_3^+ is ∼30 K (Crabtree et al. 2011a). This discrepancy is puzzling because both species are expected to be thermalized at these temperatures, just as in our model (see Fig. 1). Crabtree et al. (2011a) have shown that in contrast to H_2, the OPR of H_3^+ is likely to be non-thermal in diffuse clouds. However, the spin state of H_3^+ plays only a minor role in the spin chemistry of H_2O, as shown below.

In Fig. 2, the same plot is given for water and the water ions H_2O^+, H_3O^+. We find that the predicted OPRs deviate significantly from thermal values over the whole temperature range, i.e. 5–100 K. We can also observe that these OPRs are independent of temperature below ∼30 K. This result is reminiscent of the work of Faure et al. (2013) for the nuclear-spin chemistry of ammonia. As explained by these authors, the gas-phase OPR of NH_3 is driven by the OPR of H_2 because its direct precursor, NH_4^+, is formed through a series of hydrogen abstraction reactions with H_2. Similarly here, the direct precursor of water, H_3O^+, is mostly formed via reactions with H_2 (see reactions 2, 4, and 5). Above 30 K, the OPRs of H_2O^+, H_3O^+, and H_2O steadily increase towards their thermal value, although they do not reach it in the explored temperature range. An important finding is that the OPR of H_2O never goes below 1.5 and that it is subthermal in the range 20–100 K, with values comprised between 1.5 and 2.6. Comparisons with the observational OPRs of H_2O^+, H_3O^+, and H_2O will be presented in Section 4.

3.1.2 *H_2 OPR dependence*

It is now instructive to combine the results of Figs 1 and 2 in order to plot the OPRs of water and water ions as function of the OPR of H_2. As shown in Fig. 3, the quantity of oH_2 has no impact as long as the OPR of H_2 is lower than ∼0.1. Indeed, in this regime, the formation of the water ions follows hydrogen abstractions in a *para-rich* H_2 gas. The abundance of oH_2 starts to play a role and the OPRs of water and its ions increase significantly only when $OPR(H_2) \gtrsim 0.1$. This can be understood analytically by deriving the OPRs from the nuclear-spin branching ratios of reactions (3-6), as explained in Appendix B. Assuming that the reaction of H_3^+ with oxygen atoms is a negligible source of H_2O^+, we obtain the analytic results plotted in Fig. 3 as dotted lines. The good agreement between our reference model and the analytic calculation demonstrates that the OPR of H_2O is governed by H_2 abstractions and, consequently, by the OPR of H_2. The OPR of H_3^+ is thus found to play a minor role in the nuclear-spin chemistry of H_2O. The reaction of H_3^+ with O is, however, a significant source of OH^+.

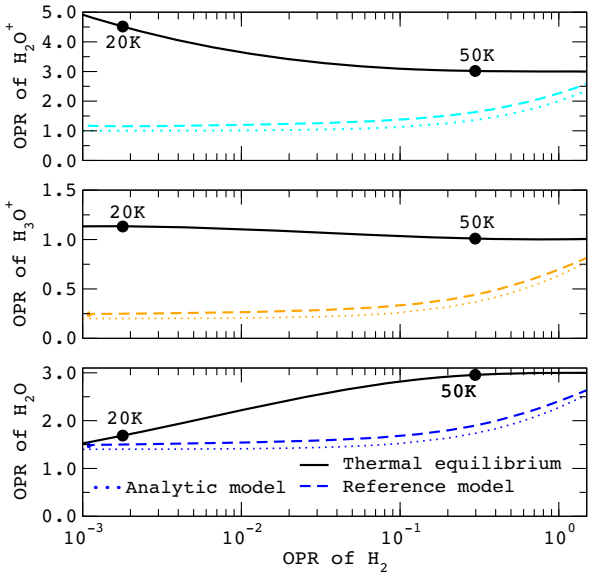

Figure 3. OPRs of H_2O^+, H_3O^+, and H_2O as function of the OPR of H_2. The solid lines give the thermalized OPRs. The dashed lines correspond to our reference model. The analytical model described in Appendix B is denoted by the dotted lines. Values of the kinetic temperature increase from left to right and are indicated at 20 and 50 K.

3.1.3 Thermalization processes

A number of thermoneutral equilibration (i.e. thermalization) processes can influence the steady-state OPR of water and its ions. These equilibration processes are neglected in the UGAN network, except the reactions of H_2 with H^+, H_3^+, and HCO^+ (and their deuterated isotopologues). We investigate in this section the impact of other possible equilibration reactions on the OPR of H_2O^+, H_3O^+, and H_2O. The kinetic temperature is varied in the range 5–50 K.

For H_2O^+, a possible equilibration reaction is

$$\mathrm{pH_2O^+ + H \leftrightarrows oH_2O^+ + H}. \quad (8)$$

It was indeed considered by Herbst (2015) in his study of the OPR of H_2O^+ in diffuse clouds. In these environments, reaction (8) can be faster than the (dominant) destruction reaction with electrons because hydrogen atoms are relatively abundant. In our reference model, however, the molecular hydrogen fraction is near unity ($[H]/[H_2] \sim 10^{-4}$) and reaction (8) is expected to be of minor importance. We have added this reaction to our network assuming that it proceeds with a rate coefficient of 2×10^{-9} cm^3 s^{-1} in the exothermic direction, i.e. near the capture (Langevin) limit. The detailed balance principle was applied for the reverse endothermic channel. The OPR of H_2O^+ was found to change by less than 0.1 per cent, meaning that reaction (8) is entirely negligible with our physical conditions.

Once water is formed, a similar equilibration reaction is

$$\mathrm{pH_2O + H^+ \leftrightarrows oH_2O + H^+}, \quad (9)$$

as suggested by Hama et al. (2018). The reaction of H_2O with protons, however, produces H_2O^+ via a strongly exothermic charge transfer with a rate coefficient of 8.2×10^{-9}cm^3 s^{-1} at room temperature (Huntress, Kim & Theard 1974). The occurrence of proton exchange in the intermediate complex H_3O^+ is therefore uncertain. Indeed, to be efficient the scrambling of hydrogen requires a sufficiently long lifetime of the intermediate complex so that many vibrations can occur before dissociation. Owing to the fast charge transfer process, scrambling is not expected to occur and reaction (9) was not considered.

Water can still exchange protons via the reaction with H_3O^+:

$$\mathrm{pH_2O + (o, p)H_3O^+ \leftrightarrows oH_2O + (o, p)H_3O^+}. \quad (10)$$

Deuterated variants of this reaction were indeed studied experimentally by Smith, Adams & Henchman (1980) at 300 K and isotope H/D exchanges were observed. The overall rate coefficient was measured as $\sim 2 \times 10^{-9}$ cm^3 s^{-1}, i.e. close to the capture limit in the average-dipole-orientation (ADO) approximation. In addition, the product distributions were found to be purely statistical, implying that the reaction proceeds via the formation of an intermediate long-lived complex. We have estimated the species-to-species rate coefficients for reaction (10) by combining the capture ADO value at 10 K ($\sim 10^{-8}$ cm^3 s^{-1}) with the simple statistical model of Rist et al. (2013). Briefly, this model is based on the density of states and it assumes that each nuclear-spin isomer lies in its lowest rotational state. The branching ratios are computed for exothermic channels (see equation 13 of Rist et al. 2013) and the detailed balance principle is applied for the reverse endothermic channels. The inclusion of reaction (10) in our network was found to change the OPR of H_2O by less than 12 per cent. This small effect reflects the fast destruction of H_2O by other abundant ions and that of H_3O^+ by electrons, which both prevent H_2O from efficiently exchanging protons with H_3O^+.

Finally, H_3O^+ could exchange protons with molecular hydrogen:

$$\mathrm{pH_3O^+ + (o, p)H_2 \leftrightarrows oH_3O^+ + (o, p)H_2}. \quad (11)$$

However, the reaction of H_3O^+ with D_2 was studied at 300 K and isotope H/D exchange was not observed, with an upper limit for the rate coefficient of 10^{-12} cm^3 s^{-1} (Kim, Theard & Huntress 1975). This was interpreted as implying that the collision of H_3O^+ with H_2 does not form a stable intermediate complex, in contrast to the reaction of H_3O^+ with H_2O. We can therefore a priori neglect the thermalization of H_3O^+ by H_2, even if H_2 is very abundant. A similar conclusion was reached by Faure et al. (2013) regarding the similar $NH_4^+ + H_2$ reaction. In order to test the potential impact of this reaction, however, we have computed species-to-species rate coefficients by combining the above upper limit (10^{-12} cm^3 s^{-1}) with the statistical model of Rist et al. (2013). Reaction (11) was found to increase the OPR of H_3O^+ by less than 1 per cent at 10 K and by about a factor of 2 at 50 K. It would be then desirable to theoretically investigate the influence of hydrogen tunnelling effects in the H_3O^+–H_2 complex.

In summary, the above equilibration reactions have a small or negligible impact on the OPR of water and water ions. This is because the destruction of these species is always faster than equilibration processes. We emphasize, however, that this result holds only for interstellar clouds where the atomic hydrogen and electron fractions are small, i.e. lower than $\sim 10^{-1}$ and $\sim 10^{-6}$, respectively.

3.1.4 Deuterated water

It is interesting to investigate the OPR of deuterated water, D_2O. As explained in Section 2.1, the chemistry of H_2O was duplicated to include most of the deuterated homologue reactions. In practice, the deuterium cloning was performed assuming that single particle (H, H^+, D, or D^+) hop is the dominant outcome of the (complex

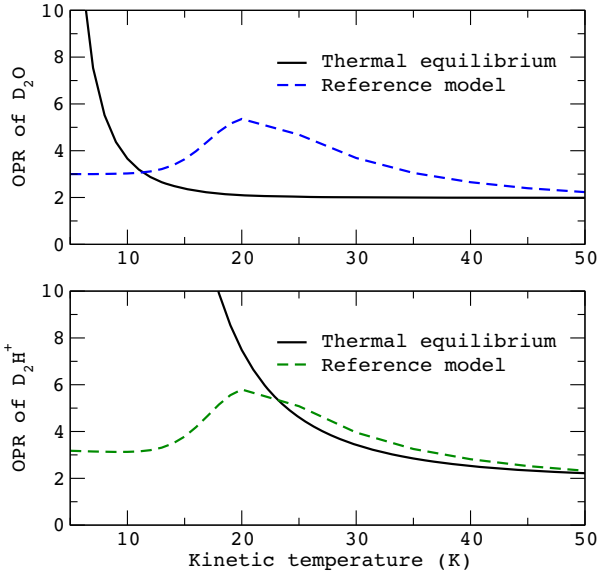

Figure 4. OPRs of D_2O and D_2H^+ as function of kinetic temperature. The solid lines give the thermalized OPRs. The dashed lines correspond to our reference model.

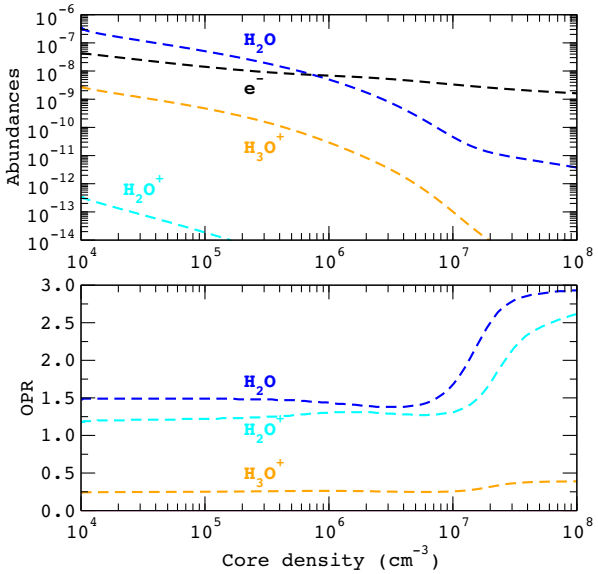

Figure 5. Top panel: evolution of the fractional abundances of H_3O^+, H_2O, H_2O^+, and electrons – expressed relative to n_H – in a cloud that is undergoing contraction in a Larson–Penston (L–P) model. Bottom panel: evolution of the OPRs of H_3O^+, H_2O^+, and H_2O in the same L–P model.

forming) reactions, as in HB18 for the ammonia chemistry. For the electronic dissociative recombination (DR) of D_2O^+ and of the deuterated isotopologues of H_3O^+, we have adopted the rate coefficients and branching ratios of H_2O^+ (Jensen et al. 1999) and H_3O^+ (Jensen et al. 2000), respectively. In addition, statistical H/D branching ratios were assumed for the products. This latter assumption is questionable because some DR experiments have suggested the occurrence of isotope (i.e. non-statistical) effects. Deviations from statistical branching ratios are however generally small. An exception is provided by the storage ring measurements of Jensen et al. (1999) on HDO^+. These authors have shown that recombination into OD + H is twice as probable as recombination into OH + D, meaning that the release of H is favoured.

The OPR of D_2O is plotted in Fig. 4 (upper panel) as a function of the kinetic temperature. It is shown to follow very closely the OPR of D_2H^+ (lower panel), which is quasi-thermalized down to 20 K due to the fast equilibration with H_2. Thus, in contrast to H_2O whose OPR is controlled by the spin state of H_2, the OPR of D_2O is driven by that of D_2H^+. This can be rationalized by considering that the gas-phase formation of D_2O proceeds through the following reactions:

$$O + D_2H^+ \rightarrow D_2O^+ + H, \quad (12)$$

$$D_2O^+ + H_2 \rightarrow HD_2O^+ + H, \quad (13)$$

$$HD_2O^+ + e^- \rightarrow D_2O + H. \quad (14)$$

The corresponding nuclear-spin branching ratios are trivial since the D_2 symmetry is conserved in these reactions. This implies that the OPR of D_2O, HD_2O^+, D_2O^+, and D_2H^+ are strictly equal. An important finding is thus that the OPR of D_2O should be a good proxy for the OPR of D_2H^+.

Observationally, the OPR of D_2O was tentatively measured in the cold envelope surrounding the protostar IRAS 16293−2422 by Vastel et al. (2010). The ground-state oD_2O and pD_2O lines were both detected in absorption and an upper limit OPR(D_2O) < 2.6 was derived, which is consistent with our chemical model only if the gas is warmer than 40 K. The analysis of these lines is however difficult, in particular because the pD_2O transition has an emission component. We note that the D_2O abundance was estimated as $\sim 10^{-11}$ (Vastel et al. 2010), which is within a factor of 2 of our prediction for $T_{kin} \sim 25$ K. Higher signal-to-noise ratio observations are clearly needed to derive a more robust OPR. The oD_2H^+ ground-state line was also detected in absorption towards IRAS 16293−2422, but not the pD_2H^+ line (Harju et al. 2017b). Lower limits OPR(D_2H^+) > 2.5 and OPR(D_2H^+) > 1.7 were derived by Harju et al. (2017b) for the envelope and the ambient cloud, respectively. These values are consistent with our model, but they do not provide additional constraints on the kinetic temperature. Future observations should help to clarify the relation between these two doubly deuterated molecules and to confirm – or disprove – the above formation path.

3.2 Larson–Penston simulation

We now investigate the fractional abundances and OPRs of H_2O and its ions during the gravitational collapse of a pre-stellar source of initial mass $M_0 = 7\,M_\odot$. The Larson–Penston (L–P) simulation assumes the same values of the cosmic ray ionization rate ($\zeta = 3 \times 10^{-17}$ s^{-1}) and the initial radius of refractory grain core ($a_g = 0.1$ μm) as in the previous calculations. The kinetic temperature is fixed at 10 K and the initial density at 10^4 cm^{-3}. Other parameters can be found in table 1 of HB18 ('reference' model). The steady-state abundances computed above (as listed in Table 1 for some species) are used as the initial composition of the collapsing sphere.

At the onset of gravitational collapse, an envelope begins to form around a core, as described in HB18. As the collapse proceeds, the core contracts and its density increases. In Fig. 5 (upper panel) are shown the variations in the fractional abundances of H_2O^+, H_3O^+, H_2O and free electrons as functions of the current density, n_H, of the core (i.e. at the interface between the core and the envelope since the core has a uniform density). As the density increases, atoms

and molecules are adsorbed by the grains, whose radius (i.e. core plus ice mantle) increases as more ice is deposited. We note that we assumed the same values $S = 1$ of the sticking coefficient for all adsorbing species. In the upper panel of Fig. 5, we observe a strong and similar decrease for the abundances of H_2O, H_2O^+, and H_3O^+ as function of the core density. This is due to the adsorption of the oxygenated species by the grains. The slower reduction of the electron abundance reflects the gas density increase ($n_e/n_H \propto n_H^{-0.5}$, see Flower, Pineau des Forêts & Walmsley 2007). At a density of 10^7 cm^{-3}, the abundances of H_2O and its ions have dropped by several orders of magnitude while that of electrons is reduced by only a factor of 10. We also observe that above a density of $\sim 10^7$ cm^{-3}, the decrease of the H_2O abundance is appreciably flatter. This can be understood by comparing the formation rates (per unit volume per unit time) of H_2O due to the DR of H_3O^+ with that due to the cosmic ray (induced and direct) desorption of water ice . At a density $n_H = 10^4$ cm^{-3}, the former is $R^{DR} \sim 7.2 \times 10^{-15}$ cm^{-3} s^{-1} while the latter is $R^{des} \sim 3.5 \times 10^{-17}$ cm^{-3} s^{-1}. At such low density, desorption is negligible. At a density $n_H = 10^7$ cm^{-3}, however, we have $R^{DR} \sim 1.9 \times 10^{-14}$ cm^{-3} s^{-1} and $R^{des} \sim 2.2 \times 10^{-14}$ cm^{-3} s^{-1} so that both formation pathways are competing. At larger density, the formation rate of gas-phase H_2O thus becomes dominated by the desorption of water ice. We have also found that cosmic ray induced photodesorption is the most efficient process: it is typically a factor of 3 faster than cosmic ray direct desorption.

This change of regime is also observed in the lower panel of Fig. 5: the OPR of H_2O is roughly constant and equal to 1.5 up to $n_H = 10^7$ cm^{-3} where it smoothly increases to reach the statistical value of 3, which is the OPR value assumed for both UV photodesorption and cosmic ray sputtering. A direct consequence is that the main formation route of H_2O^+ at high density is via the charge transfer $H_2O + H^+ \rightarrow H_2O^+ + H$. The OPR of H_2O^+ is thus found to follow that of H_2O and to slowly reach the value of 3. The OPR of H_3O^+ is, in turn, slightly increased.

Observationally, the OPR of H_2O in pre-stellar cores is unknown because only the ground-state oH_2O transition was detected in L1544 (Caselli et al. 2012). The total (ortho + para) H_2O column density was computed by these authors assuming OPR(H_2O) = 3. Since the central density of L1544 is not larger than 10^7 cm^{-3} (Keto, Rawlings & Caselli 2014), our model actually predicts that the OPR of H_2O should not exceed 1.5, implying that the column density derived by Caselli et al. (2012) would be underestimated by about 20 per cent. We finally note that our model predicts an H_2O abundance larger than 10^{-9} for $n_H \lesssim 3 \times 10^6$ cm^{-3}, which is in good agreement with the estimate by Caselli et al. (2012).

4 DISCUSSION

Our spin-state chemical model predicts that the OPRs of H_2O^+, H_3O^+, and H_2O in interstellar clouds lie in the range 1.2–2.6, 0.25–0.82, and 1.5–2.6, respectively. The ratios were found to be constant below ∼30 K and to depend essentially on the spin state of H_2. As noted above, this finding is valid for molecular clouds where the H_2 fraction f_{H_2} is close to unity and the electron fraction is lower than $\sim 10^{-6}$. We now compare these results with available observational measurements.

Observational OPRs for H_2O^+ and H_3O^+ are scarce. To our knowledge, there is only one *ISO* measurement for H_3O^+ in the Sgr B2 envelope where OPR(H_3O^+) = 0.8 ± 0.3 (Goicoechea & Cernicharo 2001). This value is consistent with the statistical value of unity, but it is also in agreement within error bars with our prediction for $T_{kin} \gtrsim 55$ K or OPR(H_2) $\gtrsim$ 0.4 (see Figs 2–3). The OPR of H_2O^+ was determined in more sources thanks to the *Herschel* satellite. In the diffuse clouds towards the Galactic centre source Sgr B2(M), it was found to be almost constant at OPR(H_2O^+) = 3.2 ± 0.4, which is consistent with the statistical ratio of 3 (Schilke et al. 2013). Herbst (2015) has shown that this is also in agreement with the formation reaction (4) if this latter proceeds by hydrogen hopping rather than by scrambling. He noticed that in such environment H_2O^+ could be also the photoionization product of H_2O desorbed from ice mantles. Similar values were derived in the diffuse clouds towards the massive star-forming regions W49N and W31C with OPR(H_2O^+) = 3.4 ± 0.6 and OPR(H_2O^+) = 2.7 ± 0.4, respectively (Gerin et al. 2013). These values are again consistent with the statistical ratio but the value in W31C is also compatible within error bars with our prediction for $T_{kin} \sim 80$ K or OPR(H_2) ∼ 1 (see Figs 2–3 and the discussion below). For both water ions, higher signal-to-noise ratios would clearly help to confirm or refute any deviation from the statistical ratios.

Many more measurements are available for interstellar H_2O thanks to *Herschel* observations. These are reported in Fig. 6 (along with the OPRs derived for comets and the protoplanetary disc TW Hya). In the ISM, the OPR values for H_2O are generally consistent with the statistical ratio of 3 within error bars. The study of Flagey et al. (2013) is the most comprehensive. In total they measured the water OPR for 13 translucent clouds. For these 13 clouds the average OPR is 2.9 ± 0.1. Of the 13 clouds, 10 have an OPR less than 3σ away from the statistical ratio. This is consistent with the model of Hollenbach et al. (2009) where most of gaseous H_2O is formed via photodesorption of water ice. One of the three other clouds has an OPR value above 3 (towards W33(A)). The OPR of the remaining two clouds is 2.3 ± 0.1 and 2.4 ± 0.2, as shown in Fig. 6. These two clouds are observed towards W49N, at velocities +40 and +60 km s^{-1}, respectively. The cloud at +40 km s^{-1} is also detected in NH_3 for which the OPR is 0.5 ± 0.3 , i.e. significantly lower than the statistical value of unity (Persson et al. 2012). As noted above, Faure et al. (2013) have shown that this low OPR is consistent with the nuclear-spin selection rules for the formation of NH_3 in a para-rich H_2 gas. Similarly here, the H_2O OPR of 2.3 ± 0.1 is predicted by our spin-state chemical model for OPR(H_2) = 0.6–1 or T_{kin} = 65–80 K (see Figs 2 and 3). It is interesting to mention that Flagey et al. (2013) have noted that this cloud is also detected in $H^{13}CO^+$ at millimetre wavelengths, suggesting that its physical properties approach those of dark clouds. A similar water OPR of 2.35 ± 0.35 was also measured in two clouds towards Sgr B2(M), at velocities < -50 km s^{-1} corresponding to the expanding molecular ring (Lis et al. 2010). A third component probably blended with the Sgr B2 envelope was also found with a low OPR of 2.3 ± 0.3 but this was attributed by Lis et al. (2010) to excitation effects. On the sightline towards Sgr B2(N), Lis et al. (2013) have also reported an average water OPR of 2.34 ± 0.25, in excellent agreement with the values found for Sgr B2(M). Finally, an even lower OPR of 1.9 ± 0.4 was derived by Choi et al. (2015) for the foreground clouds towards the high-mass protostar AFGL 2591. Such a low value is in agreement with our model for OPR(H_2) < 0.8 or T_{kin} < 70 K (see Figs 2 and 3). As noted by Choi et al. (2015), taken together these results show that water OPRs lower than 3 are found for the translucent clouds with the highest column densities, i.e. in regions where the interstellar FUV radiation field does not fully penetrate and the physical properties are close to those of dark clouds or dense cores.

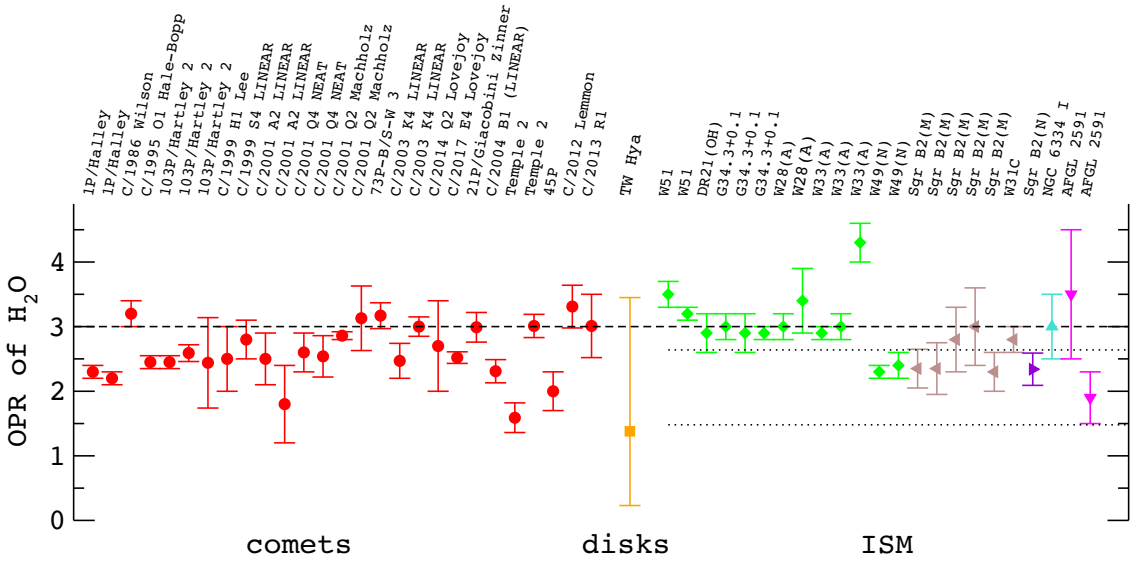

Figure 6. OPR of H_2O as measured in comets, protoplanetary discs and the ISM. References are: Faggi et al. (2018) for comets; Salinas et al. (2016) for the protoplanetary disc TW Hya (model Cm); Flagey et al. (2013) for W51, DR21(OH), G34.3 + 0.1, W28(A), W33(A), and W49(N); Lis et al. (2010) for Sgr B2(M) and W31C; Lis et al. (2013) for Sgr B2(N); Emprechtinger et al. (2013) for NGC 6334 I and Choi et al. (2015) for AFGL 2591. The black dashed line gives the statistical value of 3. The two black dotted lines correspond to our model at 10 K (OPR=1.48) and 100 K (OPR = 2.64).

In summary, *Herschel* observations have shown that the OPR of H_2O is statistical in diffuse/translucent clouds, which is consistent with models where the formation rate of gas-phase H_2O is dominated by the photodesorption of ice (Hollenbach et al. 2009). These observations also indicate that the water OPR is below the statistical value in some translucent/dense clouds and the average ratio for these sources, OPR(H_2O) $\sim$ 2.3, is consistent with the ion-neutral nuclear-spin chemistry implemented in our model (as denoted by the black dotted lines in Fig. 6). It is also possible that the FUV field is not entirely attenuated in these clouds so that the formation rate of gas-phase H_2O is $\sim$50 per cent via gas-phase reactions (with an OPR of 1.5–2) and $\sim$50 per cent by photodesorption of water ice (with an OPR of 3). The average water OPR would then be $\sim$2.2–2.5.

We can now compare these values with the water OPR reported for planetary discs and Solar system comets. To our knowledge, the first OPR measurement in a protolanetary disc was reported by Pontoppidan et al. (2010) for AS 205N using the Very Large Telescope. Their best estimate was consistent with the high-temperature limit of 3 but the low-signal-to-noise ratio precluded a robust analysis. A better measure was provided thanks to the *Herschel* observations of TW Hya by Salinas et al. (2016). These authors have reported the value OPR(H_2O) $= 1.38^{+2.07}_{-1.15}$, which has large error bars but is consistent both with the statistical ratio of 3 and the predictions of our chemical model (1.5–2.6). More accurate observations are needed to discriminate a statistical from a low OPR, which may provide an important clue to the origin of water in discs.

Finally, a large number of measurements exist for comets, as compiled recently by Faggi et al. (2018). Fig. 6 shows the OPR of water measured in 19 comets. The weighted mean, 2.60 $\pm$ 0.03, is significantly lower than 3 and the corresponding spin temperature, $\sim$31 K, is significantly lower than the typical rotational and kinetic temperatures in the coma (Bonev et al. 2013). The standard deviation (0.03), however, was computed assuming uncorrelated measurements and no systematic error. We note also that the median is 2.86. In any case, as discussed in the Introduction, the meaning of the spin temperature is under debate. The current understanding is that the OPRs in cometary comae are not indicative of the formation temperature of ices, but instead reflect either the statistical value (within uncertainties) or the gas-phase physical conditions in comae (Hama et al. 2018). Observationally, no evidence for variation of the OPR with depth in the nucleus or with nucleocentric distance in the coma has been reported (Bonev et al. 2013). A possibility is that gas-phase equilibration processes, which were found to be negligible in dark cloud conditions, play a role in the very inner coma, as discussed by Shinnaka et al. (2016). In particular, the collisions of H_2O with cold H_3O^+ ions could be an important post-sublimation nuclear-spin conversion processes. In both scenarios (statistical ratio or gas-phase processes), the spin state of cometary water would tell us nothing of the location and history of water formation.

5 CONCLUDING REMARKS

The nuclear-spin chemistry of oxygen hydrides was investigated using the UGAN chemical network updated with the most recent gas-phase kinetic data. The abundances and OPRs of gas-phase water and water ions (H_2O^+ and H_3O^+) were computed under the steady-state conditions representative of a translucent/dark molecular cloud in a large temperature range (5–100 K). The predicted abundances of OH^+, H_2O^+, H_3O^+, and H_2O were found in good agreement with the 'peak' abundances obtained by Hollenbach et al. (2009) and Hollenbach et al. (2012) in their PDR model, i.e. at $A_V \sim 5$. The OPRs of H_2O and its ions were found to deviate significantly from both thermal and statistical values and to be entirely driven by the OPR of H_2. The OPR of H_2O was shown to lie between 1.5 and 2.6 and to be consistent with values derived in translucent clouds with extinction $A_V \gtrsim 3$. Calculations were extended to the early phase of gravitational collapse of a pre-stellar core at 10 K using the dynamical model presented in HB18. The direct and indirect cosmic ray desorption processes were found to control the abundance of gas-phase water at densities $n_H \gtrsim 10^7$ cm^{-3}, where the OPR of H_2O increases from 1.5 to the statistical value of 3.

The main result of this work is that the low observational OPRs of H_2O ($\lesssim 2.5$) measured in translucent clouds are consistent with gas-phase ion-neutral chemistry *within the full scrambling hypothesis* and reflect a gas with OPR(H_2) $\lesssim 1$. Just like the OPR of NH_3 (Faure et al. 2013), the OPR of H_2O (and also its ions) therefore provides a diagnostic tool to study the 'cold' interstellar gas where H_2 is ortho-depleted (with respect to the statistical value) and difficult to detect. This tool could prove valuable in other environments such as extragalactic sources, protoplanetary discs, and comets. As discussed above, however, it should be used as a probe of local physical conditions rather than formation conditions.

More generally, the spectroscopy of ortho and para molecules in space allows to study, perhaps uniquely, the nuclear-spin conservation of identical nuclei in chemical reactions. Experimental evidence of nuclear-spin selection rules is scarce and remains to be explored in cold exothermic ion-neutral reactions, such as those involved in the synthesis of H_2O. We note in this context the recent progress in the control over the reactant quantum states in chemical reactions. Kilaj et al. (2018) were able to (spatially) separate ground-state oH_2O and pH_2O molecules which were reacted with cold N_2H^+ in an ion trap (with a $\sim$20 per cent higher reactivity for pH_2O). The control over the quantum states of both reactants and products is the next challenge. It will allow us to assess the range of applicability of the scrambling assumption, on which our results rely.

ACKNOWLEDGEMENTS

This research was supported by the CNRS national program 'Physique et Chimie du Milieu Interstellaire'. Sara Faggi and Geronimo Villanueva are acknowledged for providing the water OPRs for comets and for useful comments. We also acknowledge Emmanuel Dartois, Marin Chabot, and Eric Quirico for helpful discussions about cosmic ray sputtering experiments. Finally we thank an anonymous referee for constructive comments.

REFERENCES

Albertsson T., Indriolo N., Kreckel H., Semenov D., Crabtree K. N., Henning T., 2014, ApJ, 787, 44
Alexander C. M. O., McKeegan K. D., Altwegg K., 2018, Space Sci. Rev., 214, 36
Altwegg K. et al., 2017, Phil. Trans. R. Soc. A, 375, 20160253
Bonev B. P., Villanueva G. L., Paganini L., DiSanti M. A., Gibb E. L., Keane J. V., Meech K. J., Mumma M. J., 2013, Icarus, 222, 740
Bringa E. M., Johnson R. E., 2004, ApJ, 603, 159
Brown W. A., Bolina A. S., 2007, MNRAS, 374, 1006
Buhr H. et al., 2010, Phys. Rev. Lett., 105, 103202
Caselli P. et al., 2012, ApJ, 759, L37
Chabot M., 2016, A&A, 585, A15
Chambaud G., Levy B., Millie P., Tran Minh F., Launay J. M., Roueff E., 1980, J. Phys. B: At. Mol. Phys., 13, 4205
Choi Y., van der Tak F. F. S., van Dishoeck E. F., Herpin F., Wyrowski F., 2015, A&A, 576, A85
Cleeves L. I., Bergin E. A., Alexander C. M. O. 'D ., Du F., Graninger D., Öberg K. I., Harries T. J., 2014, Science, 345, 1590
Crabtree K. N., Indriolo N., Kreckel H., Tom B. A., McCall B. J., 2011a, ApJ, 729, 15
Crabtree K. N., Kauffman C. A., Tom B. A., Beçka E., McGuire B. A., McCall B. J., 2011b, J. Chem. Phys., 134, 194311
Dartois E. et al., 2015, A&A, 576, A125
Dislaire V., Hily-Blant P., Faure A., Maret S., Bacmann A., Pineau Des Forêts G., 2012, A&A, 537, A20
Emprechtinger M., 2013, ApJ, 765, 61
Faggi S., Villanueva G. L., Mumma M. J., Paganini L., 2018, AJ, 156, 68
Faure A., Hily-Blant P., Le Gal R., Rist C., Pineau des Forêts G., 2013, ApJ, 770, L2
Federer W., Villinger H., Howorka F., Lindinger W., Tosis P., Bassi D., Ferguson E., 1984, Phys. Rev. Lett., 52, 2084
Flagey N. et al., 2013, ApJ, 762, 11
Flower D. R., Pineau Des Forêts G., Walmsley C. M., 2005, A&A, 436, 933
Flower D. R., Pineau Des Forêts G., Walmsley C. M., 2006, A&A, 456, 215 (F06)
Flower D. R., Pineau Des Forêts G., Walmsley C. M., 2007, A&A, 474, 923
Gerin M. et al., 2013, J. Phys. Chem. A, 117, 10018
Goicoechea J. R., Cernicharo J., 2001, ApJ, 554, L213
Goldsmith P. F. et al., 2011, ApJ, 737, 96
Goto M., Geballe T. R., Usuda T., 2015, ApJ, 806, 57
Hama T., Kouchi A., Watanabe N., 2016, Science, 351, 65
Hama T., Kouchi A., Watanabe N., 2018, ApJ, 857, L13
Harju J. et al., 2017a, A&A, 600, A61
Harju J. et al., 2017b, ApJ, 840, 63
Hasegawa T. I., Herbst E., 1993, MNRAS, 261, 83
Herbst E., 2015, in EPJ Web Conf., 84, 06002
Hily-Blant P., Faure A., Rist C., Pineau des Forêts G., Flower D. R., 2018, MNRAS, 477, 4454 (HB18)
Hollenbach D., Kaufman M. J., Bergin E. A., Melnick G. J., 2009, ApJ, 690, 1497
Hollenbach D., Kaufman M. J., Neufeld D., Wolfire M., Goicoechea J. R., 2012, ApJ, 754, 105
Hugo E., Asvany O., Schlemmer S., 2009, J. Chem. Phys., 130, 164302
Huntress W. T., Jr., Kim J. K., Theard L. P., 1974, Chem. Phys. Lett., 29, 189
Indriolo N., McCall B. J., 2012, ApJ, 745, 91
Indriolo N. et al., 2015, ApJ, 800, 40
Jensen M. J., Bilodeau R. C., Heber O., Pedersen H. B., Safvan C. P., Urbain X., Zajfman D., Andersen L. H., 1999, Phys. Rev. A, 60, 2970
Jensen M. J., Bilodeau R. C., Safvan C. P., Seiersen K., Andersen L. H., Pedersen H. B., Heber O., 2000, ApJ, 543, 764
Kalvāns J., 2016, ApJS, 224, 42
Keto E., Rawlings J., Caselli P., 2014, MNRAS, 440, 2616
Kilaj A., Gao H., Rösch D., Rivero U., Küpper J., Willitsch S., 2018, Nat. Commun., 9, 2096
Kim J. K., Theard L. P., Huntress W. T., Jr., 1975, J. Chem. Phys., 62, 45
Klippenstein S. J., Georgievskii Y., McCall B. J., 2010, J. Phys. Chem. A, 114, 278
Kovalenko A., Dung Tran T., Rednyk S., Roučka Š., Dohnal P., Plašil R., Gerlich D., Glosík J., 2018, ApJ, 856, 100
Kumar S. S., Grussie F., Suleimanov Y. V., Guo H., Kreckel H., 2018, Sci. Adv., 4, eaar3417
Lacy J. H., Knacke R., Geballe T. R., Tokunaga A. T., 1994, ApJ, 428, L69
Larson R. B., 1969, MNRAS, 145, 271
Le Gal R., Hily-Blant P., Faure A., Pineau des Forêts G., Rist C., Maret S., 2014, A&A, 562, A83
Le Gal R., Xie C., Herbst E., Talbi D., Guo H., Muller S., 2017, A&A, 608, A96
Lis D. C., Bergin E. A., Schilke P., van Dishoeck E. F., 2013, J. Phys. Chem. A, 117, 9661
Lis D. C. et al., 2010, A&A, 521, L26
Léger A., Jura M., Omont A., 1985, A&A, 144, 147
McCall B. J., Geballe T. R., Hinkle K. H., Oka T., 1999, ApJ, 522, 338
Milligan D. B., McEwan M. J., 2000, Chem. Phys. Lett., 319, 482
Mumma M. J., Weaver H. A., Larson H. P., Davis D. S., Williams M., 1986, Science, 232, 1523
Neufeld D. A., Wolfire M. G., 2017, ApJ, 845, 163
Neufeld D. A. et al., 2015, ApJ, 807, 54
Oka T., 2004, J. Mol. Spectrosc., 228, 635
Penston M. V., 1969, MNRAS, 145, 457
Persson C. M. et al., 2012, A&A, 543, A145
Pontoppidan K. M., Salyk C., Blake G. A., Käufl H. U., 2010, ApJ, 722, L173
Quack M., 1977, Mol. Phys., 34, 477

Rist C., Faure A., Hily-Blant P., Le Gal R., 2013, J. Phys. Chem. A, 117, 9800
Rudd M. E., Kim Y.-K., Madison D. H., Gallagher J. W., 1985, Rev. Mod. Phys., 57, 965
Salinas V. N. et al., 2016, A&A, 591, A122
Schilke P., Lis D. C., Bergin E. A., Higgins R., Comito C., 2013, J. Phys. Chem. A, 117, 9766
Schroeder I. R. H. G. et al., 2018, European Planetary Science Congress, Berlin, Germany
Shinnaka Y., Kawakita H., Jehin E., Decock A., Hutsemékers D., Manfroid J., 2016, MNRAS, 462, S124
Smith D., Adams N. G., Henchman M. J., 1980, J. Chem. Phys., 72, 4951
Spirko J. A., Zirbel J. J., Hickman A. P., 2003, J. Phys. B: At. Mol. Phys., 36, 1645
Stancil P. C., Schultz D. R., Kimura M., Gu J.-P., Hirsch G., Buenker R. J., 1999, A&AS, 140, 225
Tran T. D., Rednyk S., Kovalenko A., Roučka Š., Dohnal P., Plašil R., Gerlich D., Glosík J., 2018, ApJ, 854, 25
Troscompt N., Faure A., Maret S., Ceccarelli C., Hily-Blant P., Wiesenfeld L., 2009, A&A, 506, 1243
Uy D., Cordonnier M., Oka T., 1997, Phys. Rev. Lett., 78, 3844
van Dishoeck E. F., Bergin E. A., Lis D. C., Lunine J. I., 2014, Protostars and Planets VI. University of Arizona Press, Tucson, p. 835
van Dishoeck E. F., Herbst E., Neufeld D. A., 2013, Chem. Rev., 113, 9043
Vastel C. et al., 2010, A&A, 521, L31
Walmsley C. M., Flower D. R., Pineau des Forêts G., 2004, A&A, 418, 1035
Webber W. R., Yushak S. M., 1983, ApJ, 275, 391
Wiesemeyer H., Güsten R., Heyminck S., Jacobs K., Menten K. M., Neufeld D. A., Requena-Torres M. A., Stutzki J., 2012, A&A, 542, L7
Ziegler J. F., Ziegler M. D., Biersack J. P., 2010, Nucl. Instrum. Methods Phys. Res. B, 268, 1818

APPENDIX A: DIRECT COSMIC RAY DESORPTION OF WATER

The direct cosmic ray desorption yield γ_{H_2O} (in molecules cm^{-2} s^{-1}) was computed by summing and integrating the product of the sputtering yield $Y_s(\epsilon, Z)$ with the differential cosmic ray flux $j(\epsilon, Z)$:

$$\gamma_{H_2O} = 4\pi \sum_Z \int_0^\infty 2Y_s(\epsilon, Z) j(\epsilon, Z) \mathrm{d}\epsilon, \tag{A1}$$

where ϵ is the kinetic energy per nucleon, Z is the atomic number of the cosmic ray nuclei and $Y_s(\epsilon, Z)$ is the 'sputtering' yield in H_2O/ion obtained by combining the experimental yield $Y_s(S_e)$ with the calculated electronic stopping power $S_e(\epsilon, Z)$. It is multiplied by a factor of 2 to account for the entrance and exit points of the cosmic rays. From their measurements and a compilation of data, Dartois et al. (2015) have fitted the experimental yield $Y_s(S_e)$ as

$$Y_s(S_e) = \alpha S_e^\beta, \tag{A2}$$

with $\alpha = 4.4^{+4.3}_{-2.2} \times 10^{-3}$, $\beta = 1.97 \pm 0.07$, and S_e^β is in units of eV/10^{15}H$_2$O cm^{-2}. The electronic stopping powers $S_e(\epsilon, Z)$ were computed with the `SRIM-2013` code[1](Ziegler, Ziegler & Biersack 2010) for a water ice density of 0.94 g cm^{-3} and for the elements with the largest contributions, taking into account the $\sim Z^4$ scaling of the sputtering yield (S_e varies as $\sim Z^2$ at high energy). This Z^4 dependence indeed largely compensates for the low abundances of heavy ions (i.e. those with $Z \geq 6$). In practice we thus included the contribution of 15 elements: H, He, C, O, Ne, Mg, Si, S, Ca, Ti, V, Cr, Mn, Fe, and Ni. Their fractional abundances $f(Z)$ with respect to hydrogen (i.e. $f(1) = 1$) were taken from the table 1 of Kalvāns (2016, see references therein). We note that iron is the species that gives the main contribution to the yield (about 40–50 per cent).

For the differential cosmic ray flux $j(\epsilon, Z)$ (in particles cm^{-2} s^{-1} sr^{-1} (MeV/amu)$^{-1}$) we adopted the functional form proposed by Webber & Yushak (1983):

$$j(\epsilon, Z) = \frac{C(Z)E^{0.3}}{(E + E_0)^3}, \tag{A3}$$

where $C(Z) = 9.42 \times 10^4 f(Z)$ is a normalizing constant and E_0 a form parameter which is between 0 and 940 MeV. The above formulation corresponds to an initial or 'primary' spectrum since it neglects the energy loss of cosmic rays through the interstellar gas. Nevertheless, it allows to explore the range of measured ionization rates from diffuse to dense clouds (see fig. 19 in Indriolo & McCall 2012) by simply varying the parameter E_0. In addition, we have found that the relation between γ_{H_2O} and ζ, as derived below, does not significantly depend on the low-energy part of $j(\epsilon, Z)$.

In order to infer the relation between γ_{H_2O} and ζ, it is necessary to compute the ionization rate ζ:

$$\zeta = 4\pi \sum_Z \int_0^\infty (1 + \Phi(\epsilon, Z))\sigma_{ion}(\epsilon, Z) j(\epsilon, Z) \mathrm{d}\epsilon, \tag{A4}$$

where $\sigma_{ion}(\epsilon, Z)$ is the ionization cross-section and $\phi(\epsilon, Z)$ is a correction factor accounting for the contribution of secondary electrons to ionization. In the Bethe–Born approximation, the ionization cross-section only depends on the atomic number Z and the velocity of the incident particle so that $\sigma_{ion}(\epsilon, Z) = Z^2 \sigma^p_{ion}(\epsilon)$ where $\sigma^p_{ion}(\epsilon)$ is the cross-section for ionization of H_2 by proton impact. In addition, the secondary electron contribution can be assumed identical for all elements and independent of energy in the relevant range (see Chabot 2016, and references therein). With the above approximations, the ionization rate becomes:

$$\zeta = 4\pi(1 + \eta)(1 + \Phi) \int_0^\infty \sigma^p_{ion}(\epsilon) j(\epsilon, 1) \mathrm{d}\epsilon, \tag{A5}$$

where

$$\eta = \sum_{Z \geq 2} f(Z) Z^2 \tag{A6}$$

is the correction factor for heavy nuclei ionization. The cross-section $\sigma^p_{ion}(\epsilon)$ was taken from Rudd et al. (1985, see their equations (31)–(33) and table III). For the secondary electron contribution we adopted the correction factor $\Phi = 0.7$ (Chabot 2016). Finally $\eta = 1.89$ was derived using the elemental abundances of Kalvāns (2016). It should be noted that all other ionization processes, including electron capture, were neglected because their contribution to the ionization rate was found to be less than 1 per cent for the chosen cosmic ray differential flux. In practice, the E_0 parameter in equation (A3) was varied between 100 and 900 MeV so that ζ was explored in the range 8×10^{-18}–2×10^{-15}. The integrals in equations (A1) and (A5) were evaluated numerically from $\epsilon_{min} = 100$ eV amu^{-1} to $\epsilon_{max} = 10$ GeV amu^{-1}. It should be noted that the low-energy part (<100 MeV) of the cosmic ray spectrum is poorly constrained (Chabot 2016) and leads to large uncertainties in the ionization rate. On the other hand, we have found that the relation between γ_{H_2O} and ζ is quite robust. The calibration is plotted in Fig. A1 and one can notice that the relation is very close to linear ($\gamma_{H_2O} \propto \zeta^{1.07}$). We suggest therefore to use the simple linear relation:

$$\gamma_{H_2O} = 0.8 \left(\frac{\zeta}{10^{-17} \mathrm{s}^{-1}} \right), \tag{A7}$$

[1] http://www.srim.org.

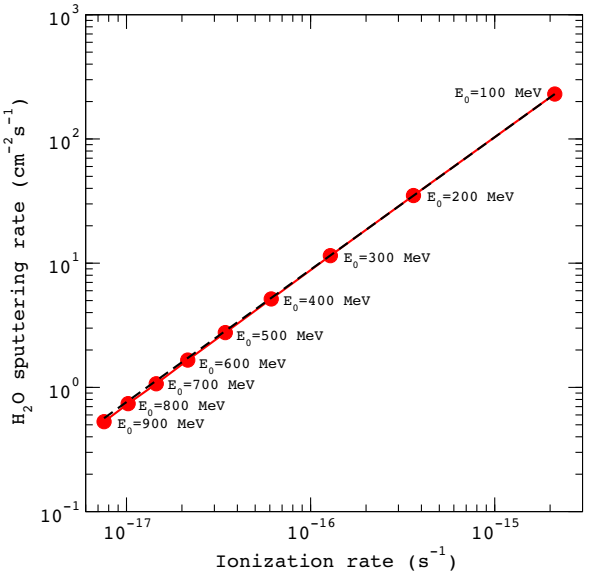

Figure A1. Water sputtering rate γ_{H_2O} (in molecules cm^{-2} s^{-1}) as function of the ionization rate ζ. The data points are computed from equations (A1) and (A5) with the form parameter E_0 varied from 100 to 900 MeV. The dashed line gives a least-squares fit $a(\zeta/10^{-17}\mathrm{s}^{-1})^b$ with $a = 0.76$ and $b = 1.07$.

for ζ in the range $\sim 10^{-17}$–10^{-15} s^{-1}.

Finally, it is instructive to estimate the time-scale for cosmic ray hits. Taking $E_0 = 600$ MeV (i.e. $\zeta = 2.2 \times 10^{-17}$ s^{-1}) with a fractional abundance of iron of 4.6×10^{-4}, the time between impacts for a grain of radius $a = 0.1$ μm is

$$t_{\rm CR} = \left(4\pi^2 a^2 \int_0^\infty j(\epsilon, 26)\mathrm{d}\epsilon\right)^{-1} \sim 2 \times 10^4 \text{ yr}, \tag{A8}$$

which means that over the lifetime of a pre-stellar core ($\sim 10^6$ yr) a grain will experience about 50 impacts.

APPENDIX B: ANALYTIC ORTHO-TO-PARA RATIO OF H_2O

We derive below the OPR of water and water ions following their formation via the reaction of OH^+ and H_2O^+ with H_2 and the DR of H_3O^+ with electrons. We will assume (i) that the reactivities of *para*- and *ortho*-species are identical (i.e. same overall formation and destruction rates) and (ii) that the destruction rates are faster than equilibration (thermalization) processes. With these two hypotheses, the OPRs of H_2O^+, H_3O^+, and H_2O are controlled by the formation paths. We will also assume that all reactions proceed via the full scrambling of protons in long-lived complexes.

Let us first consider the formation of oH_2O^+ and pH_2O^+ through the reaction of OH^+ with pH_2 and oH_2. Nuclear-spin branching ratios can be derived using the approaches of Oka (2004) or Quack (1977):

$$\mathrm{OH^+ + pH_2} \rightarrow \begin{cases} \mathrm{pH_2O^+ + H}\ \frac{1}{2} \\ \mathrm{oH_2O^+ + H}\ \frac{1}{2} \end{cases} \tag{B1}$$

$$\mathrm{OH^+ + oH_2} \rightarrow \begin{cases} \mathrm{pH_2O^+ + H}\ \frac{1}{6} \\ \mathrm{oH_2O^+ + H}\ \frac{5}{6} \end{cases} \tag{B2}$$

From the above equations we derive easily:

$$\mathrm{OPR(H_2O^+)} = \frac{\frac{1}{2} + \frac{5}{6}\mathrm{OPR(H_2)}}{\frac{1}{2} + \frac{1}{6}\mathrm{OPR(H_2)}}. \tag{B3}$$

Likewise, by combining equation (B3) with the nuclear-spin branching ratios for the formation of H_3O^+:

$$\mathrm{pH_2O^+ + pH_2} \rightarrow \begin{cases} \mathrm{pH_3O^+ + H}\ 1 \\ \mathrm{oH_3O^+ + H}\ 0 \end{cases} \tag{B4}$$

$$\mathrm{pH_2O^+ + oH_2} \rightarrow \begin{cases} \mathrm{pH_3O^+ + H}\ \frac{2}{3} \\ \mathrm{oH_3O^+ + H}\ \frac{1}{3} \end{cases} \tag{B5}$$

$$\mathrm{oH_2O^+ + pH_2} \rightarrow \begin{cases} \mathrm{pH_3O^+ + H}\ \frac{2}{3} \\ \mathrm{oH_3O^+ + H}\ \frac{1}{3} \end{cases} \tag{B6}$$

$$\mathrm{oH_2O^+ + oH_2} \rightarrow \begin{cases} \mathrm{pH_3O^+ + H}\ \frac{1}{3} \\ \mathrm{oH_3O^+ + H}\ \frac{2}{3} \end{cases} \tag{B7}$$

we obtain:

$$\mathrm{OPR(H_3O^+)} = \frac{\frac{1}{6} + \mathrm{OPR(H_2)}[\frac{7}{9} + \frac{11}{18}\mathrm{OPR(H_2)}]}{\frac{5}{6} + \mathrm{OPR(H_2)}[\frac{11}{9} + \frac{7}{18}\mathrm{OPR(H_2)}]}. \tag{B8}$$

By combining equation (B8) with the branching ratios for the DR of H_3O^+:

$$\mathrm{pH_3O^+ + e^-} \rightarrow \begin{cases} \mathrm{pH_2O + H}\ \frac{1}{2} \\ \mathrm{oH_2O + H}\ \frac{1}{2} \end{cases} \tag{B9}$$

$$\mathrm{oH_3O^+ + e^-} \rightarrow \begin{cases} \mathrm{pH_2O + H}\ 0 \\ \mathrm{oH_2O + H}\ 1 \end{cases} \tag{B10}$$

we finally obtain:

$$\mathrm{OPR(H_2O)} = 2\mathrm{OPR(H_3O^+)} + 1 \tag{B11}$$

$$= \frac{\frac{1}{3} + 2\mathrm{OPR(H_2)}[\frac{7}{9} + \frac{11}{18}\mathrm{OPR(H_2)}]}{\frac{5}{6} + \mathrm{OPR(H_2)}[\frac{11}{9} + \frac{7}{18}\mathrm{OPR(H_2)}]} + 1\,. \tag{B12}$$

The above equations (B3), (B8), and (B12) are used in Fig. 3 to plot the 'analytical' OPRs as function of the OPR of H_2. We note that if $\mathrm{OPR(H_2)} = 3$, these equations predict that $\mathrm{OPR(H_2O^+)} = 3$, $\mathrm{OPR(H_3O^+)} = 1$ and $\mathrm{OPR(H_2O)} = 3$, as expected in the statistical limit. On the other hand, if $\mathrm{OPR(H_2)} \ll 1$, they predict $\mathrm{OPR(H_2O^+)} = 1$, $\mathrm{OPR(H_3O^+)} = 1/5$ and $\mathrm{OPR(H_2O)} = 7/5$, as observed in Fig. 3 (see the dotted lines).

As can be noticed in Fig. 3, the above equations slightly underestimate the OPRs predicted by our reference model. This can be explained by the reaction of O with H_3^+ which is another (secondary) source of H_2O^+. It can be easily shown from the following branching ratios:

$$\mathrm{O + pH_3^+} \rightarrow \begin{cases} \mathrm{pH_2O^+ + H}\ \frac{1}{2} \\ \mathrm{oH_2O^+ + H}\ \frac{1}{2} \end{cases} \tag{B13}$$

$$\mathrm{O + oH_3^+} \rightarrow \begin{cases} \mathrm{pH_2O^+ + H}\ 0 \\ \mathrm{oH_2O^+ + H}\ 1 \end{cases} \tag{B14}$$

that the corresponding OPR of H_2O^+ is

$$\mathrm{OPR(H_2O^+)} = 2\mathrm{OPR(H_3^+)} + 1\,. \tag{B15}$$

Thus, at low $\mathrm{OPR(H_2)}$ where $\mathrm{OPR(H_3^+)} \sim 0.4$ (see Fig. 1) this reaction produces $\mathrm{OPR(H_2O^+)} \sim 1.8$, which explains why the actual OPR of H_2O^+ is slightly above unity. The OPRs of H_3O^+ and H_2O are in turn slightly above 1/5 and 7/5, respectively.

This paper has been typeset from a TEX/LATEX file prepared by the author.